PHYSICAL REVIEW MATERIALS **6**, 054201 (2022)

Observation of nontrivial topological electronic structure of orthorhombic SnSe

H. J. Zheng,[1,2] W. J. Shi,[3] C. W. Wang,[1,2] Y. Y. Lv,[4,5] W. Xia,[1,6] B. H. Li,[1] F. Wu,[1] S. M. He,[7] K. Huang,[1,2] S. T. Cui,[8]
C. Chen,[7,9] H. F. Yang,[1] A. J. Liang,[1,6] M. X. Wang,[1,6] Z. Sun,[8] S. H. Yao,[4,5] Y. B. Chen,[4,5] Y. F. Guo,[1,6]
Q. X. Mi,[1] L. X. Yang,[10] M. S. Bahramy,[11] Z. K. Liu,[1,6,*] and Y. L. Chen[1,6,7,10,†]
[1] *School of Physical Science and Technology, ShanghaiTech University, Shanghai 201210, People's Republic of China*
[2] *University of Chinese Academy of Sciences, Beijing 100049, People's Republic of China*
[3] *Center for Transformative Science, and Shanghai High Repetition Rate XFEL and Extreme Light Facility (SHINE), ShanghaiTech University, Shanghai 201210, People's Republic of China*
[4] *Department of Physics, Department of Materials Science and Engineering, National Laboratory of Solid State Microstructures, Nanjing University, Nanjing 210093, People's Republic of China*
[5] *Collaborative Innovation Center of Advanced Microstructures, Nanjing University, Nanjing 210093, People's Republic of China*
[6] *ShanghaiTech Laboratory for Topological Physics, Shanghai 201210, People's Republic of China*
[7] *Department of Physics, University of Oxford, Oxford OX1 3PU, United Kingdom*
[8] *National Synchrotron Radiation Laboratory, University of Science and Technology of China, Hefei, Anhui 230026, People's Republic of China*
[9] *Advanced Light Source, Lawrence Berkeley National Laboratory, Berkeley, California 94720, USA*
[10] *State Key Laboratory of Low Dimensional Quantum Physics, Department of Physics, Tsinghua University, Beijing 100084, People's Republic of China*
[11] *Department of Physics and Astronomy, The University of Manchester, Manchester M13 9PL, United Kingdom*

(Received 5 February 2022; accepted 14 April 2022; published 5 May 2022)

Topological electronic structures are key to the topological classification of quantum materials and play an important role in their physical properties and applications. Recently, SnSe has attracted great research interest due to its superior thermoelectric performance. However, its topological nature has long been ignored. In this work, by combining synchrotron-based angle-resolved photoemission spectroscopy and *ab initio* calculations, we systematically investigate the topological electronic structure of orthorhombic SnSe. By identifying the continuous gap in the valence bands due to the band inversion and the topological surface states on its (001) surface, we establish SnSe as a strong topological insulator. Furthermore, we study the evolution of the topological electronic structure and propose the topological phase diagram in $SnSe_{1-x}Te_x$. Our work reveals the topological nontrivial nature of SnSe and provides understandings of its intriguing transport properties.

DOI: 10.1103/PhysRevMaterials.6.054201

I. INTRODUCTION

Topological phases of matter have attracted extensive research interest in the condensed matter physics field [1–3]. Over the past decade, numerous types of topological materials have been theoretically proposed by first-principles calculation and experimentally verified by transport or spectroscopic measurements. The category now includes topological insulators [1–3], three-dimensional topological Dirac and Weyl semimetals [4–6], topological superconductors [2,7–12], and topological magnetic insulators/semimetals [13–16]. The recent rapid development of high-throughput prediction of band topology based on the theories of topological quantum chemistry [17] and symmetry-based indicators [18–21] provides us a more efficient approach to search for the topological materials with application potentials.

Similar to the well-studied topological insulators Bi_2Se_3 and Bi_2Te_3 [22–24], the group-IV monochalcogenides family and their alloys are known as promising thermoelectric materials [25–27]. Among them, SnSe hosts the record-high thermoelectric figure of merit of ~2.6 at 923K [25], much higher than that of typical known high-performance thermoelectric materials [28–30]. Previous investigations on the electronic structure of SnSe have focused on its impact on thermoelectric properties, and revealed valence bands with multiple valleys and relatively small in-plane effective masses, which are key to the enhancement of the Seebeck coefficient while keeping high electrical conductivity [31–34]. These angle-resolved photoemission spectroscopy (ARPES) works not only provide deeper understanding of the electronic origin of the excellent thermoelectric properties in SnSe, but also offer a guideline for improving higher-*ZT* thermoelectric materials by band structure engineering. However, the topological aspect of SnSe has long been ignored. SnSe has two isomers: The metastable SnSe with rocksalt crystal structure (similar to SnTe) was theoretically proposed to be a topological crystalline insulator (TCI) [35],

---

[*] yulin.chen@physics.ox.ac.uk
[†] liuzhk@shanghaitech.edu.cn

and experimentally confirmed by angle-resolved photoemission spectroscopy (ARPES) in epitaxial grown films [36,37]. The thermodynamically more stable SnSe with a layered orthorhombic (*Pnma*, No. 62) GeS-type crystal structure [27,38] has long been considered as a topologically trivial band insulator with gap size ~0.9 eV [39]. Although a pressure-induced superconducting transition and topological phase transition were experimentally observed [40], direct evidence of topological electronic structure of SnSe has not been addressed from the previous spectroscopic works [31–34,41].

In this work, we present systematic investigation on the electronic structure of orthorhombic SnSe, by combining the use of state-of-the-art ARPES technique and *ab initio* calculations. Based on the detailed theoretical analysis of the topological invariant and systematic photon-energy-dependent ARPES measurement, we identified the nontrivial topological electronic structure of SnSe, including a continuous gap in the valence bands due to the band inversion and topological surface states (TSSs) within the continuous gap on its (001) surface, thus proving SnSe as a strong topological insulator (STI). Different from most other topological insulators with TSSs inside the bulk gap such as Bi_2Se_3/Bi_2Te_3 [1–3,23], the TSSs of orthorhombic SnSe are buried deeply below the Fermi energy (E_F) and strongly overlap with the bulk valence band, demonstrating its unusual robustness. In addition, our investigation on the evolution of the band structure of $SnSe_{1-x}Te_x$ ($x = 0$, 0.2, and 0.5) demonstrates the band evolution under different spin-orbit coupling (SOC) strengths, where the topological nontrivial electronic structures persist. Our result further suggests a topological phase transition (STI to TCI) accompanying the structural phase transition with $x > 0.7$ [42]. Our work deepens the understanding on the topological nature of the SnSe family and sheds light on further understanding of its electronic structure and thermoelectric properties [43,44].

II. METHODS

SnSe and $SnSe_{1-x}Te_x$ single crystals were grown by the vapor transport method. We first synthesize the polycrystalline samples by the direct solid-state reaction using stoichiometric quantities of Sn (99.995%, Alfa Aesar), Se (99.999%, Alfa Aesar), and Te (99.999%, Alfa Aesar). In detail, the starting materials were loaded in a preheated quartz ampoule inside the glove box, sealed under vacuum (10^{-4} Pa), heated to 950 °C at 12 h, and held for 36 h to obtain polycrystalline samples. Then the amounts of polycrystalline powders were mixed with iodine (I_2, transport agent, 2.5 mg/cm^3) and transferred in another sealed and evacuated (10^{-4} Pa) quartz ampoule. A two-zone tube furnace was used with a temperature gradient of 100 °C between hot (source temperature, 600 °C) and cold (growth temperature, 500 °C) zones to grow crystals. Over 10 days of transport, many single crystals shaped as thin plates were obtained at the cold part of the quartz ampoule.

Synchrotron-based ARPES measurements were performed at beamline 13U of the National Synchrotron Radiation Laboratory (NSRL), China, and beamline 03U of the Shanghai Synchrotron Radiation Facility (SSRF), China [45]. The samples were cleaved *in situ* and measured under ultrahigh vacuum below 5×10^{-11} Torr. Data were collected by a Scienta DA30L analyzer. The total energy and angle resolution were below 10 meV and 0.2°, respectively.

The first-principles calculations were carried out using the Vienna *ab initio* simulation package (VASP) [46]. The valence electrons and ion core interactions were described by the projector augmented wave (PAW) method [47,48]. The exchange-correlation potential is formulated by the generalized gradient approximation with the Perdew-Burke-Ernzerhof (PBE) scheme [49]. The Γ-centered $12 \times 12 \times 4$ k points are used for the first Brillouin-zone sampling. The plane-wave basis cutoff energy is set to 300 eV. The tight-binding Hamiltonian was constructed using the maximally localized Wannier function which was provided by the WANNIER90 package [50]. The projected atomic s and p orbitals of the Sn and Se atoms were employed to reproduce the *ab initio* calculated band structure. The surface states were obtained by the surface Green's function method [51]. The experiment lattice constant (Inorganic Crystal Structure Database No. 12863) was used in the calculations. In the unit cell of SnSe, there are four Sn and four Se atoms. For $SnSe_{0.75}Te_{0.25}$, one Se atom was substituted by one Te atom, while for $SnSe_{0.5}Te_{0.5}$, two Se atoms were substituted by two Te atoms. After relaxation, the structures with the lowest energy were used for the following calculation.

III. RESULTS AND DISCUSSIONS

As shown in Figs. 1(a)–1(c), orthorhombic phase SnSe adopts a layered crystal structure of space group *Pnma* with inversion symmetry [38], which can be viewed as a binary analogy to the isostructural black phosphorus, an intriguing two-dimensional (2D) material with prominent carrier mobility, thickness-dependent direct band gap, and in-plane anisotropic physical properties [52–55]. Each layer consists of a puckered honeycomb lattice of alternating Sn and Se atoms, with armchair chains along the x axis and zigzag chains along the y axis. The adjacent layers have the opposite direction along the x axis. The crystal naturally cleaves along the (001) direction, which is ideal for the ARPES measurements. The high quality of the crystals used in this work was confirmed by x-ray diffraction (Fig. S1 of the Supplemental Material [56]). The bulk Brillouin zone (BZ) and the projected (001) surface BZs are shown in Fig. 1(d), with the high-symmetry points labeled.

We first carry out detailed density functional theory (DFT) calculations to identify the topological nature of the compound. Figures 1(e) and 1(f) show the calculated bulk band structure of orthorhombic SnSe without and with SOC, respectively. In addition to the indirect bulk band gap of about 0.9 eV [39] of SnSe, we can observe the turning on of a "continuous gap" [shaded in gray in Fig. 1(f)] in which there is no crossing of the bulk valence bands after the inclusion of strong SOC, together with band inversions of Sn-s and Se-p orbitals as labeled in Fig. 1(f). We evaluate the topological nature of the compound based on the inversion symmetry of the crystal, by using the method proposed by Fu and Kane [57]. As shown in Fig. 1(d), the eight time-reversal-invariant momenta (TRIM) points in the BZ are Γ, X, S, Y, Z, U, T, and R, respectively. Since the other six TRIM points have the

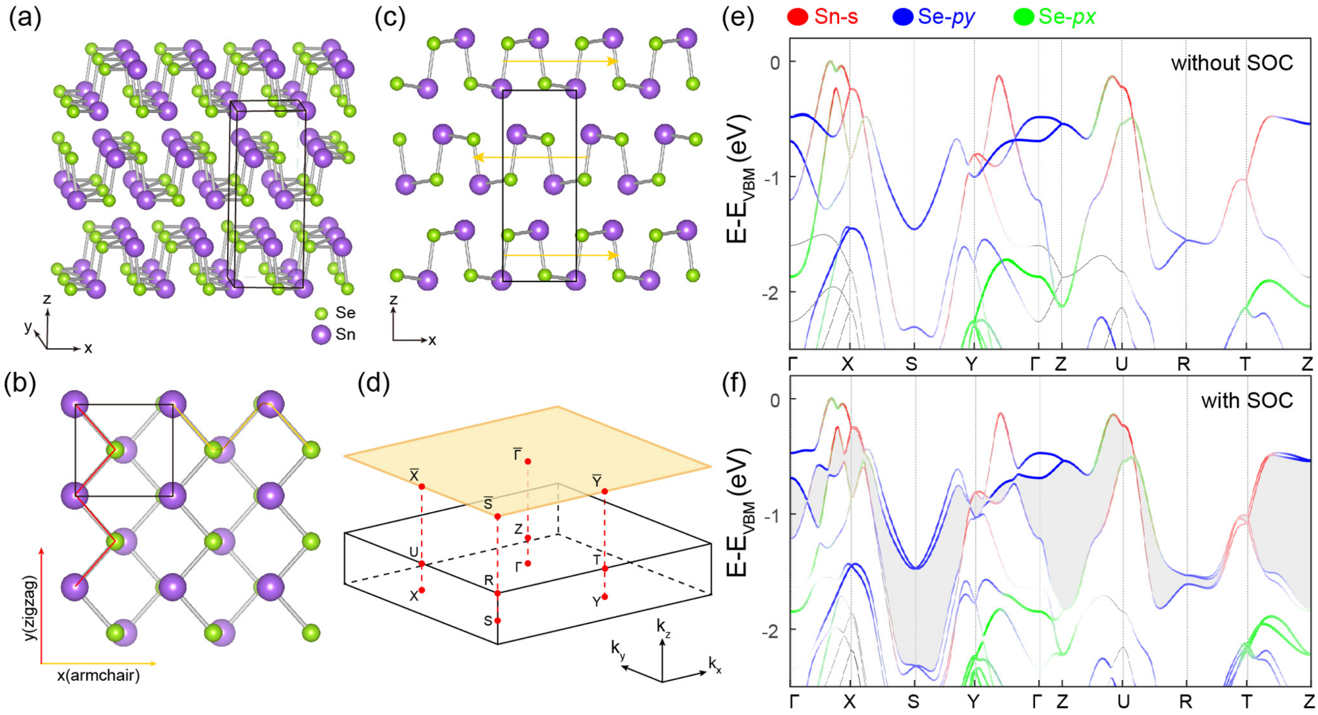

FIG. 1. Crystal structure and bulk band structure calculation. (a) 3D view of layered orthorhombic crystal structure of thermodynamically stable orthorhombic phase SnSe. (b) Top view of a SnSe layer; zigzag and armchair chains are labeled by red and yellow lines. (c) Side view perpendicular to the armchair direction, showing two adjacent layers having the opposite direction along the x axis. (d) The corresponding 3D Brillouin zone (BZ) of SnSe and its projected surface BZ to (001) surface, with high-symmetry points labeled. (e), (f) First-principles band calculations without and with spin-orbit coupling (SOC), respectively. Gray shaded area in (f) shows the continuous gap induced by SOC. Red, blue, and green dots indicate the Sn-s, Se-py, and Se-px orbital contributions, respectively.

same parities, the Z_2 invariant ν_0 can be calculated by considering parities of Γ and T points solely, resulting in $\nu_0 = 1$. The result suggests the orthorhombic SnSe is an STI which has been ignored in previous reports [31–34,41]. Further, we explicitly unveil the characteristic TSS in SnSe by calculating the spectral function of the (001) surface using the semi-infinite surface model (details in Part II of the Supplemental Material [56]). As shown in Fig. 2(a), multiple nontrivial TSSs have been predicted inside the continuous gap of SnSe, as highlighted in red. The most prominent one can be found around the $\bar{X}$ point along the $\bar{\Gamma} - \bar{X}$ direction.

We verify the predicted topologically nontrivial electronic structure by performing synchrotron-based ARPES measurements. The overall measured electronic structure of SnSe on the (001) surface is illustrated in Fig. 2(b). The photoemission spectra are recorded by using $\mathbf{h}\nu = 21$ eV photons, roughly corresponding to the $k_z = 0$ case (the detailed relationship between photon energies and k_z has been reported in our previous work [32]). Figure 2(b) presents the measured electronic band structure in the three-dimensional (3D) volume plot containing both the $\bar{\Gamma}$ and $\bar{X}$ points at the BZ boundary, showing overall agreement with the *ab initio* calculations (a detailed comparison is also presented in Ref. [32]).

As shown in Figs. 2(d-i) and 2(e-i), in order to examine the topological character of the electronic structures, we zoom in on the band dispersions along the high-symmetry $\bar{\Gamma} - \bar{X}$ and $\bar{\mathrm{X}} - \bar{S}$ directions. The major features are contributed by the four topmost bulk valence bands α, β_1, β_2, and γ, and an obvious SOC-induced gap between β_1 and β_2 was observed in Fig. 2(d-i), which is predicted to be a band crossing at ~ 0.1 Å^{-1} away from $\bar{X}$ along the $\bar{\Gamma} - \bar{X}$ direction without SOC [Fig. 1(c)]. Interestingly, the α and β_1 bands, as well as the β_2 and γ bands, are degenerate at the $\bar{X}$ point. According to the *ab initio* calculation, the degenerations along the $\bar{X} - \bar{S}$ line without SOC [Fig. 1(c)] are lifted with SOC [Figs. 1(d) and 2(e-ii)]. Unfortunately, these degeneration liftings cannot be clearly distinguished within our energy resolution, possibly due to the strong k_z broadening effect [58]. We further address the topological surface state by making a detailed comparison of the measured band dispersions and the semi-infinite surface calculations in Figs. 2(d-iii) and 2(e-iii), and observe an excellent agreement. The TSSs near the $\bar{X}$ predicted by the calculation were clearly seen in experimental band dispersions as in gap (i.e., the continuous gap) states connecting the β_1 and β_2 bands. They appear as a flat “X” shape along the $\bar{\Gamma} - \bar{X}$ direction [Fig. 2(d)] and are much more dispersed along the $\bar{X} - \bar{S}$ direction between the β_1 and β_2 bands. The existence of the TSSs can also be evidenced in the constant energy contours at the 0.4 eV below the Fermi level [Fig. 2(c)]. The dispersion of another TSS could be observed at a deeper binding energy in the ARPES measurement along the $\bar{X} - \bar{S}$ direction [Fig. 2(e)].

We probe the surface nature of the observed TSSs by photon-energy-dependent ARPES measurements using photon energies from 19 to 29 eV, covering more than half of the bulk BZ [32]. As shown in Fig. 3, the TSSs observed along

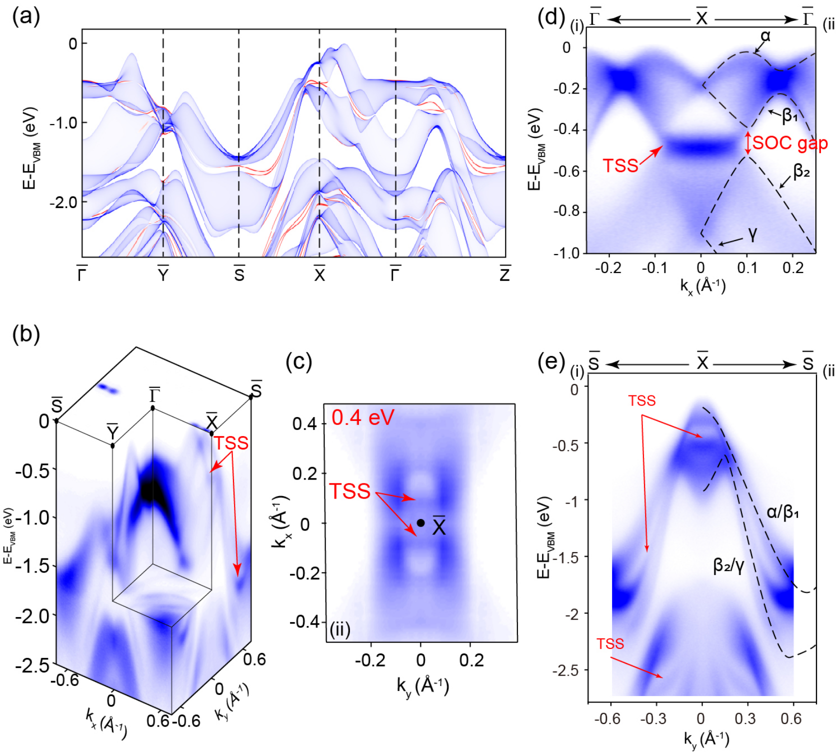

FIG. 2. Observation of topological surface states on SnSe (001) surface. (a) The calculation result shown along the high-symmetry lines of the surface Brillouin zone. Topological surface states are clearly visible and highlighted in red. (b) A 3D intensity plot of the photoemission spectra around the $\bar{X}$ point with TSS indicated by red arrows. (c) Spectral intensity plot showing constant energy contours around the $\bar{X}$ point at $E - E_{\mathrm{VBM}} = 0.4\,\mathrm{eV}$. (d), (e) Photoemission intensity (left panel), and corresponding *ab initio* bulk (middle panel) and semi-infinite surface (right panel) calculation along the high-symmetry $\bar{\Gamma} - \bar{X}$ (d) and $\bar{S} - \bar{X}$ (e) directions. The TSSs are indicated by the red arrows in (i) and highlighted in red in (iii).

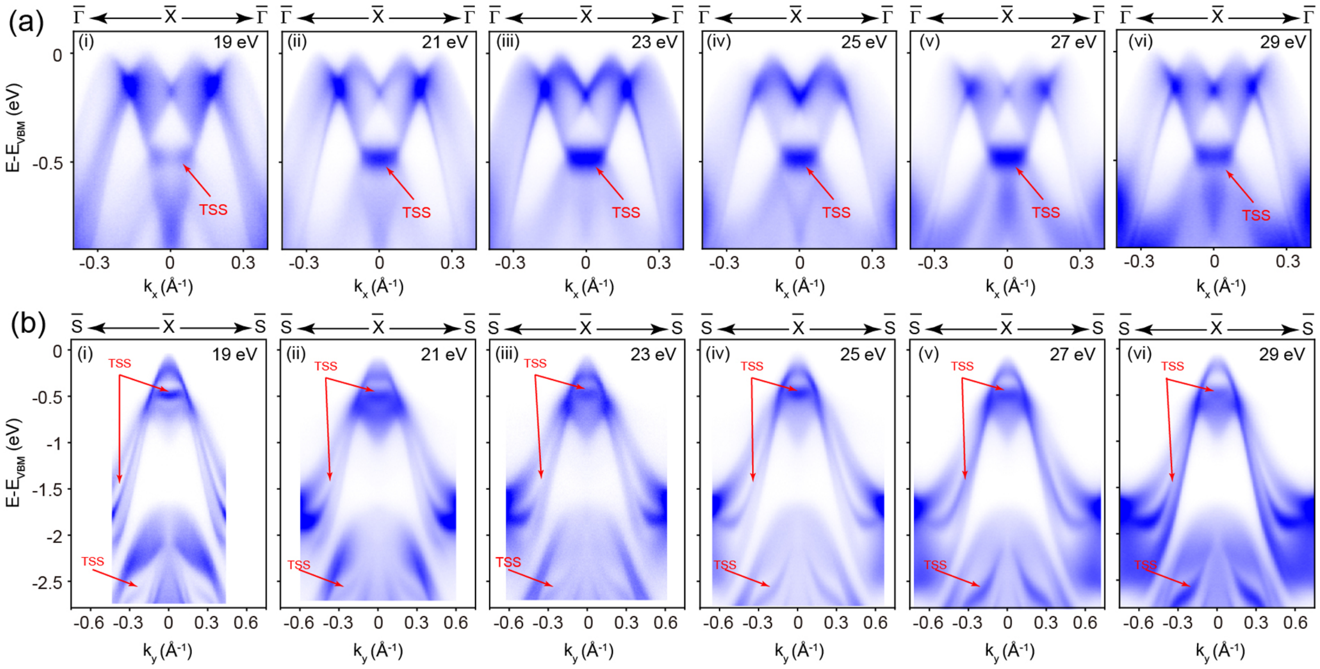

FIG. 3. Photon energy dependence of the TSS on SnSe (001) surface. (a,b) Photoemission intensity plot along the high-symmetry $\bar{\Gamma} - \bar{X}$ (a) and $\bar{S} - \bar{X}$ (b) directions with photon energies from 19 to 29 eV covering more than half the bulk BZ. Red arrows indicate TSSs that do not change with the photon energies, although the transition matrix element effects modulate the intensity shape of TSS captured by different photons.

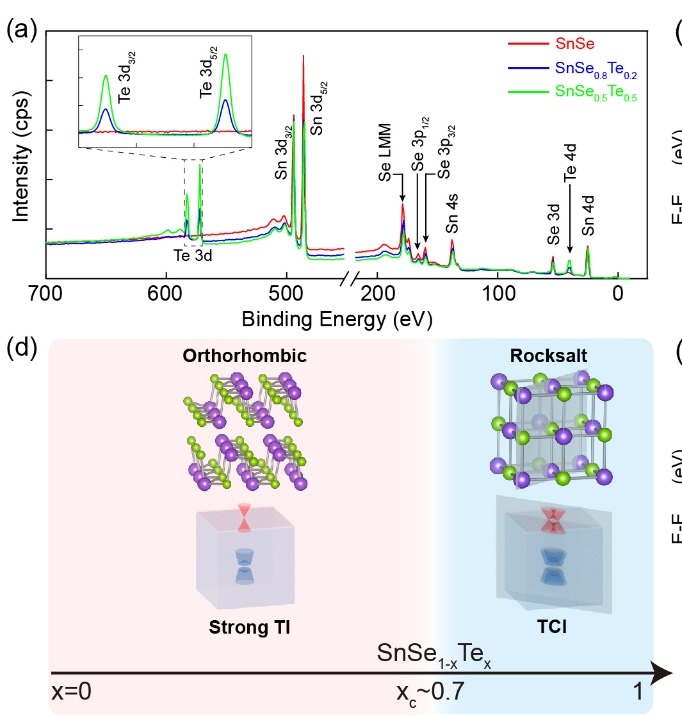

FIG. 4. Evolution of the band structure of SnSe with different tellurium doping amounts. (a) The x-ray photoelectron spectra (XPS) of SnSe, $SnSe_{0.8}Te_{0.2}$, and $SnSe_{0.5}Te_{0.5}$ clearly show their characteristic core level peaks. Zoomed-in plot of Te 3*d* doublets indicates different contents of Te element in three compounds. (b), (c) Comparison of measured band dispersions (upper panel) and corresponding calculated band structures (lower panel) around the $\bar{X}$ point for SnSe, $SnSe_{0.8}Te_{0.2}$, and $SnSe_{0.5}Te_{0.5}$, respectively. The TSSs are highlighted in red in (c). (d) Sketch of a structural and topological phase transition across a critical point x_c in $SnSe_{1-x}Te_x$.

both the $\bar{\Gamma}-\bar{Y}$ and $\bar{Y}-\bar{S}$ directions show little variations in the dispersion under all photon energies, clearly demonstrating the absence of $k_\perp$ dispersion of the TSSs.

We further investigate the evolution of the topological nontrivial electronic structure of $SnSe_{1-x}Te_x$ with Te substituting Se. $SnSe_{1-x}Te_x$ remains a stable orthorhombic crystal structure up to $x = 0.5$ before the structural transition to the rocksalt phase [42]. In Fig. 4(a), the x-ray photoelectron spectra (XPS) of three x values (SnSe, $SnSe_{0.8}Te_{0.2}$, and $SnSe_{0.5}Te_{0.5}$) clearly show characteristic core level peaks of Se, Te, and Sn, which suggest their high crystal quality and differences in chemical compositions, respectively. With the increase of Te composition, as evidenced by the growing peak of Te 3*d* doublets [the zoomed-in plot of Fig. 4(a)], the SOC strength should be enhanced. With the stronger SOC and Te substitution the electronic structure of $SnSe_{1-x}Te_x$ experiences complex evolution, the continuous gap deforms but still remains, and the TSS survives, as predicted by the semi-infinite surface calculations [Figs. 4(e)–4(g)]. Our ARPES measurement of $SnSe_{0.8}Te_{0.2}$ and $SnSe_{0.5}Te_{0.5}$ nicely repeats the predicted band structure [Figs. 4(b)–4(d)], where the observed inner electron pocket of the topmost valence band moves to deeper binding energy compared to the SnSe case. The TSS becomes deeply buried in the bulk continuum and can no longer be distinguished. Our calculation and ARPES measurement, along with previously reported TCI in SnTe [59], suggest the $SnSe_{1-x}Te_x$ hosts a strong topological insulator phase across a wide x range before experiencing the structural [42] and topological phase transition into the rocksalt/topological crystalline insulator phase [Fig. 4(d)].

Our observation of the unusual TSSs in orthorhombic phase SnSe establish it as the first example with nontrivial topological electronic structure in the group-IV monochalcogenide family crystallizing into the thermal-stable orthorhombic phase, instead of the metastable rocksalt phase. The *ab initio* calculation and following parity criterion based Z_2 invariant analysis accurately identify it as a strong topological insulator. The deeply buried TSSs show unusual robustness as they strongly overlap with bulk bands and survive under Te substitution, which suggests the possibility to utilize the TSS in potential electronic applications.

The result on $SnSe_{1-x}Te_x$ also suggests great tunability in band structure engineering, providing a great platform to understand the interplay between the crystalline symmetry, SOC strength, electronic structure, and thermoelectric property [43,44,60]. The rich topological phenomena in the group-IV monochalcogenide family makes them an interesting playground for the realization of novel topological effects and topological phases. In addition, the electronic structure and related topological nature near the critical point of the structural and topological phase transition in $SnSe_{1-x}Te_x$ merit further investigations.

ACKNOWLEDGMENT

This work is sponsored by the National Key R&D Program of China (Grant No. 2017YFA0305400 to Z.K.L.).

[1] M. Hasan and C. Kane, Colloquium: Topological insulators, Rev. Mod. Phys. **82**, 3045 (2010).
[2] X.-L. Qi and S.-C. Zhang, Topological insulators and superconductors, Rev. Mod. Phys. **83**, 1057 (2011).
[3] Y. Ando, Topological insulator materials, J. Phys. Soc. Jpn. **82**, 102001 (2013).
[4] N. P. Armitage, E. J. Mele, and A. Vishwanath, Weyl and Dirac semimetals in three-dimensional solids, Rev. Mod. Phys. **90**, 015001 (2018).
[5] B. Yan and C. Felser, Topological materials: Weyl semimetals, Annu. Rev. Condens. Matter Phys. **8**, 337 (2017).
[6] B. Q. Lv, T. Qian, and H. Ding, Experimental perspective on three-dimensional topological semimetals, Rev. Mod. Phys. **93**, 025002 (2021).
[7] C. Nayak, S. H. Simon, A. Stern, M. Freedman, and S. D. Sarma, Non-Abelian anyons and topological quantum computation, Rev. Mod. Phys. **80**, 1083 (2008).
[8] M. Sato and Y. Ando, Topological superconductors: A review, Rep. Prog. Phys. **80**, 076501 (2017).
[9] P. Zhang, K. Yaji, T. Hashimoto, Y. Ota, T. Kondo, K. Okazaki, Z. Wang, J. Wen, G. Gu, H. Ding, and S. Shin, Observation of topological superconductivity on the surface of an iron-based superconductor, Science **360**, eaan4596 (2018).
[10] Y. Fang, J. Pan, D. Zhang, D. Wang, H. T. Hirose, T. Terashima, S. Uji, Y. Yuan, W. Li, Z. Tian, J. Xue, Y. Ma, W. Zhao, Q. Xue, G. Mu, H. Zhang, and F. Huang, Discovery of superconductivity in 2M WS_2 with possible topological surface states, Adv. Mater. **31**, 1901942 (2019).
[11] Y. W. Li, H. J. Zheng, Y. Q. Fang, D. Q. Zhang, Y. J. Chen, C. Chen, A. J. Liang, W. J. Shi, D. Pei, L. X. Xu, S. Liu, J. Pan, D. H. Lu, M. Hashimoto, A. Barinov, S. W. Jung, C. Cacho, M. X. Wang, Y. He, L. Fu *et al.*, Observation of topological superconductivity in a stoichiometric transition metal dichalcogenide 2M-WS_2, Nat. Commun. **12**, 2874 (2021).
[12] Y. Yuan, J. Pan, X. Wang, Y. Fang, C. Song, L. Wang, K. He, X. Ma, H. Zhang, F. Huang, W. Li, and Q.-K. Xue, Evidence of anisotropic Majorana bound states in 2M-WS_2, Nat. Phys. **15**, 1046 (2019) .
[13] Y. Tokura, K. Yasuda, and A. Tsukazaki, Magnetic topological insulators, Nat. Rev. Phys. **1**, 126 (2019).
[14] Y. J. Chen, L. X. Xu, J. H. Li, Y. W. Li, H. Y. Wang, C. F. Zhang, H. Li, Y. Wu, A. J. Liang, C. Chen, S. W. Jung, C. Cacho, Y. H. Mao, S. Liu, M. X. Wang, Y. F. Guo, Y. Xu, Z. K. Liu, L. X. Yang, and Y. L. Chen, Topological Electronic Structure and Its Temperature Evolution in Antiferromagnetic Topological Insulator $MnBi_2Te_4$, Phys. Rev. X **9**, 041040 (2019).
[15] Y.-J. Hao, P. Liu, Y. Feng, X.-M. Ma, E. F. Schwier, M. Arita, S. Kumar, C. Hu, R. Lu, M. Zeng, Y. Wang, Z. Hao, H.-Y. Sun, K. Zhang, J. Mei, N. Ni, L. Wu, K. Shimada, C. Chen, Q. Liu *et al.*, Gapless Surface Dirac Cone in Antiferromagnetic Topological Insulator $MnBi_2Te_4$, Phys. Rev. X **9**, 041038 (2019).
[16] D. F. Liu, A. J. Liang, E. K. Liu, Q. N. Xu, Y. W. Li, C. Chen, D. Pei, W. J. Shi, S. K. Mo, P. Dudin, T. Kim, C. Cacho, G. Li, Y. Sun, L. X. Yang, Z. K. Liu, S. S. P. Parkin, C. Felser, and Y. L. Chen, Magnetic Weyl semimetal phase in a kagomé crystal, Science **365**, 1282 (2019).
[17] B. Bradlyn, L. Elcoro, J. Cano, M. G. Vergniory, Z. Wang, C. Felser, M. I. Aroyo, and B. A. Bernevig, Topological quantum chemistry, Nature (London) **547**, 298 (2017).
[18] M. G. Vergniory, L. Elcoro, C. Felser, N. Regnault, B. A. Bernevig, and Z. Wang, A complete catalogue of high-quality topological materials, Nature (London) **566**, 480 (2019).
[19] T. Zhang, Y. Jiang, Z. Song, H. Huang, Y. He, Z. Fang, H. Weng, and C. Fang, Catalogue of topological electronic materials, Nature (London) **566**, 475 (2019).
[20] J. Kruthoff, J. de Boer, J. van Wezel, C. L. Kane, and R.-J. Slager, Topological Classification of Crystalline Insulators through Band Structure Combinatorics, Phys. Rev. X **7**, 041069 (2017).
[21] R.-J. Slager, A. Mesaros, V. Juričić, and J. Zaanen, The space group classification of topological band-insulators, Nat. Phys. **9**, 98 (2013).
[22] H. Zhang, C.-X. Liu, X.-L. Qi, X. Dai, Z. Fang, and S.-C. Zhang, Topological insulators in Bi_2Se_3, Bi_2Te_3 and Sb_2Te_3 with a single Dirac cone on the surface, Nat. Phys. **5**, 438 (2009).
[23] Y. L. Chen, J. G. Analytis, J.-H. Chu, Z. K. Liu, S.-K. Mo, X. L. Qi, H. J. Zhang, D. H. Lu, X. Dai, Z. Fang, S. C. Zhang, I. R. Fisher, Z. Hussain, and Z.-X. Shen, Experimental realization of a three-dimensional topological insulator, Bi_2Te_3, Science **325**, 178 (2009).
[24] Y. Xia, D. Qian, D. Hsieh, L. Wray, A. Pal, H. Lin, A. Bansil, D. Grauer, Y. Hor, R. Cava, and M. Hasan, Observation of a large-gap topological-insulator class with a single Dirac cone on the surface, Nat. Phys. **5**, 398 (2009).
[25] L.-D. Zhao, S.-H. Lo, Y. Zhang, H. Sun, G. Tan, C. Uher, C. Wolverton, V. P. Dravid, and M. G. Kanatzidis, Ultralow thermal conductivity and high thermoelectric figure of merit in SnSe crystals, Nature (London) **508**, 373 (2014).
[26] L.-D. Zhao, G. Tan, S. Hao, J. He, Y. Pei, H. Chi, H. Wang, S. Gong, H. Xu, V. P. Dravid, C. Uher, G. J. Snyder, C. Wolverton, and M. G. Kanatzidis, Ultrahigh power factor and thermoelectric performance in hole-doped single-crystal SnSe, Science **351**, 141 (2016).
[27] Z.-G. Chen, X. Shi, L.-D. Zhao, and J. Zou, High-performance SnSe thermoelectric materials: Progress and future challenge, Prog. Mater Sci. **97**, 283 (2018).
[28] K. Biswas, J. He, I. D. Blum, C.-I. Wu, T. P. Hogan, D. N. Seidman, V. P. Dravid, and M. G. Kanatzidis, High-performance bulk thermoelectrics with all-scale hierarchical architectures, Nature (London) **489**, 414 (2012).
[29] H. J. Wu, L.-D. Zhao, F. S. Zheng, D. Wu, Y. L. Pei, X. Tong, M. G. Kanatzidis, and J. Q. He, Broad temperature plateau for thermoelectric figure of merit $ZT > 2$ in phase-separated $PbTe_{0.7}S_{0.3}$, Nat. Commun. **5**, 4515 (2014).
[30] S. I. Kim, K. H. Lee, H. A. Mun, H. S. Kim, S. W. Hwang, J. W. Roh, D. J. Yang, W. H. Shin, X. S. Li, Y. H. Lee, G. J. Snyder, and S. W. Kim, Dense dislocation arrays embedded in grain boundaries for high-performance bulk thermoelectrics, Science **348**, 109 (2015).
[31] Q. Lu, M. Wu, D. Wu, C. Chang, Y.-P. Guo, C.-S. Zhou, W. Li, X.-M. Ma, G. Wang, L.-D. Zhao, L. Huang, C. Liu, and J. He, Unexpected Large Hole Effective Masses in SnSe Revealed by Angle-Resolved Photoemission Spectroscopy, Phys. Rev. Lett. **119**, 116401 (2017).
[32] C. W. Wang, Y. Y. Y. Xia, Z. Tian, J. Jiang, B. H. Li, S. T. Cui, H. F. Yang, A. J. Liang, X. Y. Zhan, G. H. Hong, S. Liu, C. Chen, M. X. Wang, L. X. Yang, Z. Liu, Q. X. Mi, G. Li, J. M. Xue, Z. K. Liu, and Y. L. Chen, Photoemission study of

the electronic structure of valence band convergent SnSe, Phys. Rev. B **96**, 165118 (2017).

[33] Z. Wang, C. Fan, Z. Shen, C. Hua, Q. Hu, F. Sheng, Y. Lu, H. Fang, Z. Qiu, J. Lu, Z. Liu, W. Liu, Y. Huang, Z.-A. Xu, D. W. Shen, and Y. Zheng, Defects controlled hole doping and multivalley transport in SnSe single crystals, Nat. Commun. **9**, 47 (2018).

[34] I. Pletikosić, F. von Rohr, P. Pervan, P. K. Das, I. Vobornik, R. J. Cava, and T. Valla, Band Structure of the IV-VI Black Phosphorus Analog and Thermoelectric SnSe, Phys. Rev. Lett. **120**, 156403 (2018).

[35] Y. Sun, Z. Zhong, T. Shirakawa, C. Franchini, D. Li, Y. Li, S. Yunoki, and X.-Q. Chen, Rocksalt SnS and SnSe: Native topological crystalline insulators, Phys. Rev. B **88**, 235122 (2013).

[36] Z. Wang, J. Wang, Y. Zang, Q. Zhang, J. Shi, T. Jiang, Y. Gong, C. Song, S. Ji, L. Wang, L. Gu, K. He, W. Duan, X. Ma, X. Chen, and Q. Xue, Molecular beam epitaxy-grown SnSe in the rock-salt structure: An artificial topological crystalline insulator material, Adv. Mater. **27**, 4150 (2015).

[37] W. Jin, S. Vishwanath, J. Liu, L. Kong, R. Lou, Z. Dai, J. T. Sadowski, X. Liu, H.-H. Lien, A. Chaney, Y. Han, M. Cao, J. Ma, T. Qian, S. Wang, M. Dobrowolska, J. Furdyna, D. A. Muller, K. Pohl, H. Ding *et al.*, Electronic Structure of the Metastable Epitaxial Rock-Salt SnSe {111} Topological Crystalline Insulator, Phys. Rev. X **7**, 041020 (2017).

[38] P. Wu, Y. Ishikawa, M. Hagihala, S. Lee, K. Peng, G. Wang, S. Torii, and T. Kamiyama, Crystal structure of high-performance thermoelectric materials by high resolution neutron powder diffraction, Phys. B (Amsterdam) **551**, 64 (2018).

[39] M. Parenteau and C. Carlone, Influence of temperature and pressure on the electronic transitions in SnS and SnSe semiconductors, Phys. Rev. B **41**, 5227 (1990).

[40] X. Chen, P. Lu, X. Wang, Y. Zhou, C. An, Y. Zhou, C. Xian, H. Gao, Z. Guo, C. Park, B. Hou, K. Peng, X. Zhou, J. Sun, Y. Xiong, Z. Yang, D. Xing, and Y. Zhang, Topological Dirac line nodes and superconductivity coexist in SnSe at high pressure, Phys. Rev. B **96**, 165123 (2017).

[41] K. Zhang, K. Deng, J. Li, H. Zhang, W. Yao, J. Denlinger, Y. Wu, W. Duan, and S. Zhou, Widely tunable band gap in a multivalley semiconductor SnSe by potassium doping, Phys. Rev. Materials **2**, 054603 (2018).

[42] J. Shen, J. M. Woods, Y. Xie, M. D. Morales-Acosta, and J. J. Cha, Structural phase transition and carrier density tuning in $\mathrm{SnSe}_x\mathrm{Te}_{1-x}$ nanoplates, Adv. Electron. Mater. **2**, 1600144 (2016).

[43] C. Fu, Y. Sun, and C. Felser, Topological thermoelectrics, APL Mater. **8**, 040913 (2020).

[44] Y. Xu, Z. Gan, and S.-C. Zhang, Enhanced Thermoelectric Performance and Anomalous Seebeck Effects in Topological Insulators, Phys. Rev. Lett. **112**, 226801 (2014).

[45] Y.-C. Yang, Z.-T. Liu, J.-S. Liu, Z.-H. Liu, W.-L. Liu, X.-L. Lu, H.-P. Mei, A. Li, M. Ye, S. Qiao, and D.-W. Shen, High-resolution ARPES endstation for *in situ* electronic structure investigations at SSRF, Nucl. Sci. Tech. **32**, 31 (2021).

[46] G. Kresse and J. Furthmüller, Efficient iterative schemes for *ab initio* total-energy calculations using a plane-wave basis set, Phys. Rev. B **54**, 11169 (1996).

[47] P. E. Blöchl, Projector augmented-wave method, Phys. Rev. B **50**, 17953 (1994).

[48] G. Kresse and D. Joubert, From ultrasoft pseudopotentials to the projector augmented-wave method, Phys. Rev. B **59**, 1758 (1999).

[49] J. P. Perdew, K. Burke, and M. Ernzerhof, Generalized Gradient Approximation Made Simple, Phys. Rev. Lett. **77**, 3865 (1996).

[50] I. Souza, N. Marzari, and D. Vanderbilt, Maximally localized Wannier functions for entangled energy bands, Phys. Rev. B **65**, 035109 (2001).

[51] M. P. L. Sancho, J. M. L. Sancho, J. M. L. Sancho, and J. Rubio, Highly convergent schemes for the calculation of bulk and surface green functions, J. Phys. F: Met. Phys. **15**, 851 (1985).

[52] X. Ling, H. Wang, S. Huang, F. Xia, and M. S. Dresselhaus, The renaissance of black phosphorus, Proc. Natl. Acad. Sci. USA **112**, 4523 (2015).

[53] L. Li, Y. Yu, G. J. Ye, Q. Ge, X. Ou, H. Wu, D. Feng, X. H. Chen, and Y. Zhang, Black phosphorus field-effect transistors, Nat. Nanotechnol. **9**, 372 (2014).

[54] B. Deng, V. Tran, Y. Xie, H. Jiang, C. Li, Q. Guo, X. Wang, H. Tian, S. J. Koester, H. Wang, J. J. Cha, Q. Xia, L. Yang, and F. Xia, Efficient electrical control of thin-film black phosphorus bandgap, Nat. Commun. **8**, 14474 (2017).

[55] J. Qiao, X. Kong, Z.-X. Hu, F. Yang, and W. Ji, High-mobility transport anisotropy and linear dichroism in few-layer black phosphorus, Nat. Commun. **5**, 4475 (2014).

[56] See Supplemental Material at http://link.aps.org/supplemental/10.1103/PhysRevMaterials.6.054201 for details of the materials and methods, and the supplemental text.

[57] L. Fu and C. L. Kane, Topological insulators with inversion symmetry, Phys. Rev. B **76**, 045302 (2007).

[58] J. A. Sobota, Y. He, and Z.-X. Shen, Angle-resolved photoemission studies of quantum materials, Rev. Mod. Phys. **93**, 025006 (2021).

[59] Y. Tanaka, Z. Ren, T. Sato, K. Nakayama, S. Souma, T. Takahashi, K. Segawa, and Y. Ando, Experimental realization of a topological crystalline insulator in SnTe, Nat. Phys. **8**, 800 (2012).

[60] L. Müchler, F. Casper, B. Yan, S. Chadov, and C. Felser, Topological insulators and thermoelectric materials, Phys. Status Solidi RRL **7**, 91 (2013).